

# MEMS, Field-Emitter, Thermal, Fluidic Devices

A Tabletop Deep Reactive Ion Etching System for MEMS Development and Production .....	101
A Miniature MEMS Vacuum Pump with Curved Electrostatic Actuation.....	102
Additive Manufacturing of Three-Dimensional Microfluidics.....	103
Piezoelectric Nonlinearity in GaN Lamb Mode Resonators .....	104
Controlled Fabrication of Nanoscale Gaps using Stiction .....	105
Printed MEMS Membrane Electrostatic Microspeakers .....	106
Electromagnetic Imaging of Nanostructures.....	107
Purification of High Salinity Brine by Multi-Stage Desalination via Ion Concentration Polarization (ICP) .....	108
Enhanced Flow Boiling in Microchannels via Incorporated Surface Structures.....	109
Experimental Characterization of Thin-Film Evaporation from Silicon Micropillar Wicks.....	110
Elementary Framework for Cold Field Emission: Emission from Quantum-Confined Emitters .....	111
High-Throughput Manufacturing of Nanofibers using Planar Arrays of Microfabricated Externally Fed Emitters.....	112
Optimization of the Morphology of Arrays of Nano-Sharp, Photon-Triggered Silicon Field Emitters to Maximize their Total Current Emission .....	113
Advanced X-Ray Sources for Absorption Imaging of Low-Z Materials.....	114
A Field Emission-Based Ultra-High Vacuum Pump for Cold-Atom Interferometry Systems.....	115

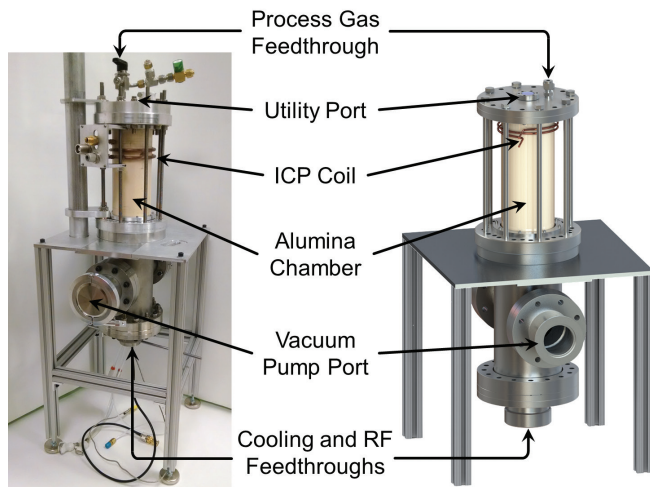


# A Tabletop Deep Reactive Ion Etching System for MEMS Development and Production

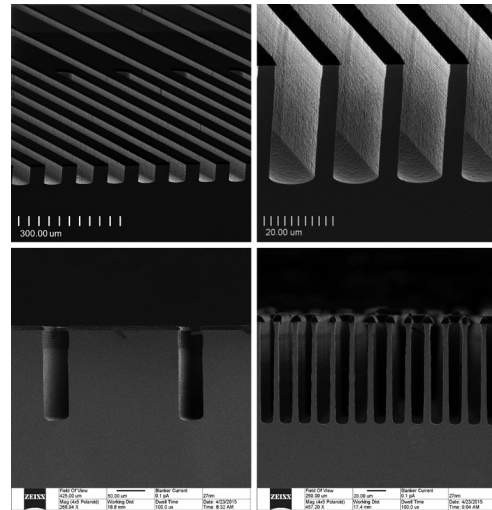
P. A. Gould, M. D. Hsing, K. K. Gleason, M. A. Schmidt  
Sponsorship: MTL

A general rule of thumb for new semiconductor fabrication facilities (fabs) is that revenues from the first year of production must match the capital cost of building the fab itself. With modern fabs routinely exceeding \$1 billion to build, this rule serves as a significant barrier to entry for groups seeking to commercialize new semiconductor devices aimed at smaller market segments that require a dedicated process. To eliminate this cost barrier, we are working to create a suite of tools that will process small (~1") substrates and cost less than \$1 million. This suite of tools, known colloquially as the 1" Fab, offers many advantages over traditional fabs. By shrinking the size of the substrate, we can realize substantial savings in material usage, energy consumption, and, most importantly, capital costs. This substantial reduction in capital costs will drastically increase the availability of semiconductor fabrication technology and enable experimentation, prototyping, and small-scale production to occur locally and economically.

The first 1" Fab tool we have developed is a deep reactive ion etcher (DRIE). DRIE tools are used to create highly anisotropic, high aspect-ratio trenches in silicon—a crucial element in many MEMS processes that will benefit from a 1" Fab platform. A labeled image and rendering of the 1" Fab DRIE is shown in Figure 1. The modularized design of our DRIE system can be easily adapted to produce other plasma-based etching and deposition tools (like PECVD and RIE). Using the switched-mode Bosch Process, the 1" Fab DRIE system currently can achieve silicon etch rates up to 6  $\mu\text{m}/\text{min}$  with vertical sidewall profiles, an estimated photoresist selectivity greater than 50:1, and etch depth non-uniformity to less than 2% across the substrate. Several examples of anisotropic etches performed with our system are included in Figure 2. Presently, we are working to refine the mechanical design of the system and optimizing recipes for high-aspect ratio etching.



▲ Figure 1: View of the basic components of the 1" Fab DRIE system.



▲ Figure 2: Examples of anisotropic etches performed using the Bosch Process in the 1" Fab DRIE.

## FURTHER READING

- S. Heck, S. Kaza, and D. Pinner. (2011, Autumn). Creating value in the semiconductor industry [Online]. Available: [http://www.mckinsey.com/~/media/McKinsey/dotcom/client\\_service/Semiconductors/PDFs/MOSC\\_1\\_Value\\_creation.ashx](http://www.mckinsey.com/~/media/McKinsey/dotcom/client_service/Semiconductors/PDFs/MOSC_1_Value_creation.ashx).
- F. Laermer and A. Schilp, "Method of anisotropically etching silicon," U. S. Patent 5,501,893, March 26, 1996.

# A Miniature MEMS Vacuum Pump with Curved Electrostatic Actuation

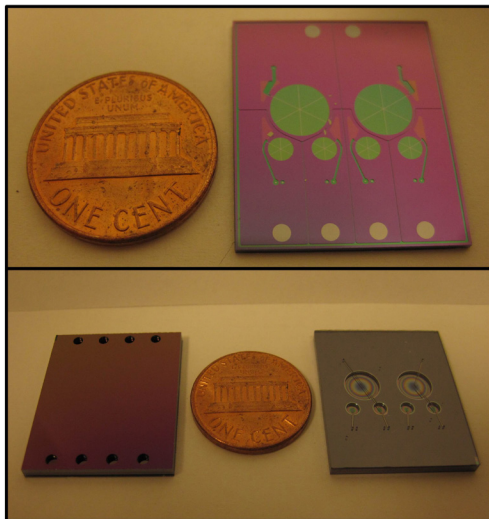
E. Newton, H. Li, M. A. Schmidt  
Sponsorship: DARPA

Portable sensing devices such as microscale mass spectrometers need vacuum pumping to lower samples at atmospheric pressure to the desired measurement pressure range. Further improvements for MEMS accelerometers, gyros, and other resonant sensors require internal pressures as low as a few microrr, which is possible only with active vacuum pumping. While these pressures are easily achieved using macroscale vacuum pumps, the larger pumps are not portable, negating the benefits gained from making small, low-power sensors in the first place. To realize the full potential of portable sensors, a chip-scale vacuum pump needs to be developed.

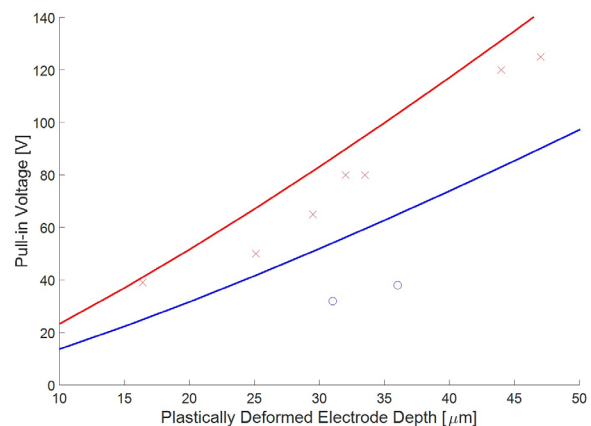
We are developing what is to our knowledge the first two-stage MEMS displacement pump with integrated electrostatic actuation. Two pump stages, along with an efficient layout that minimizes dead volume and a new actuation scheme, should enable it to reach pressures below 30 Torr. Actuation is achieved by electrostatically

zipping a thin flexible membrane down onto a stiff curved electrode. This actuator topology allows for large displacements and large forces at relatively low voltages (< 100 V). An image of a fabricated two-stage micropump is shown in Figure 1 below.

We have developed two methods for producing curved electrodes in MEMS devices: 1) hot air trapped during wafer bonding expands with enough pressure to plastically deform a thin silicon membrane and 2) strain induced when epoxy cures can pull a membrane into a curved shape. We have demonstrated that we can reliably and repeatably zip a thin membrane using these curved electrodes at low voltages and we have mapped out how the critical voltage depends on the deformation magnitude and the oxide thickness. Finally, we have developed models to predict the extent of plastic deformation and the onset of pullin for these curved electrostatic electrodes. A comparison of the model and experimental data is shown in Figure 2 below.



▲ Figure 1: Microfabricated two-stage vacuum pump. Top and bottom views of the pumps are shown (bottom), as are internal fluidic connections (top).



▲ Figure 2: Pull-in voltages for 6-mm-diameter curved electrodes with a 25- $\mu\text{m}$ -thick zipping membrane. Data are shown for a 0.1- $\mu\text{m}$  gap (blue) and a 0.5- $\mu\text{m}$  gap (red).

## FURTHER READING

- H. Zhou, H. Q. Li, V. Sharma, and M. A. Schmidt, "A single-stage micromachined vacuum pump achieving 164 torr absolute pressure," in 2011 *IEEE 24th International Conference on Micro Electro Mechanical Systems*, 2011, pp. 1095-1098.
- M. A. Huff, A. D. Nikolich, and M. A. Schmidt, "Design of Sealed Cavity Microstructures Formed by Silicon Wafer Bonding," *Journal of Microelectromechanical Systems*, vol. 2, pp. 74-81, June 1993.

# Additive Manufacturing of Three-Dimensional Microfluidics

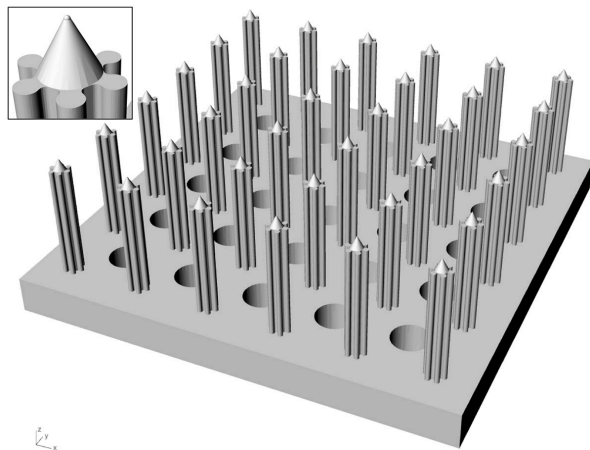
L. F. Velásquez-García  
Sponsorship: DARPA

In many cases, microfluidics are manufactured in clean-rooms using semiconductor industry processes and materials, making them fairly expensive to produce. In addition, the device architecture is often a compromise between what should be made based on modeling and what can be made based on the planarity and thickness/depth limitation of most microfabrication processes. Moreover, a change of any of the in-plane features of the design typically requires the fabrication of one or more new lithography masks, incurring substantial costs and time delays. A manufacturing technology that can circumvent these difficulties without sacrificing device performance would greatly extend the kind of devices that can be made and the kind of commercial applications beyond research, high-end products, and large-volume products that can be satisfied by microfluidic chips.

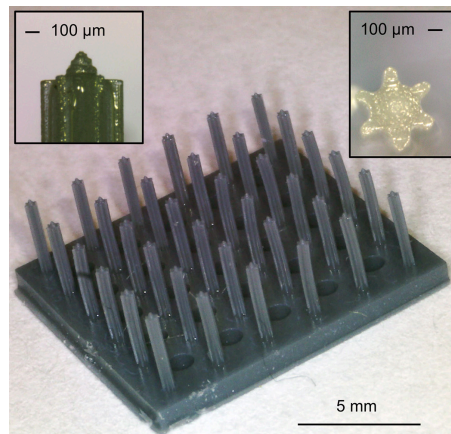
Additive manufacturing is a group of layer-by-layer fabrication methods that use a computer file to generate solid objects. Additive manufacturing started as a visualization tool of passive, mesoscaled parts; however, given the recent improvements in the resolution

capabilities and cost of commercial 3D printers, additive manufacturing has recently been explored as a fabrication technology that could address the complexity of certain microsystems, e.g., microfluidics.

We are exploring the use of stereolithography to manufacture freeform microfluidics with three-dimensional hydraulic networks with features (range of dimensions, aspect ratio, morphology) that would be very hard to make using standard microfabrication processing. Stereolithography is an additive fabrication process that uses a computer file (Figure 1) to manufacture structures based on spatially controlled solidification of a liquid resin by photo-polymerization. For example, we have developed fabrication process flows for the creation of three-dimensional structures that can be used as multiplexed, externally fed electro spray emitter arrays (Figure 2); these structures have a minimum feature size and emitter density comparable to reported single-crystal silicon multiplexed electro spray devices. Current work focuses on exploring the resolution limits and capabilities of the 3D printing process, as well as in demonstrating working microfluidic chips.



▲ Figure 1: Computer-aided design file of a monolithic array of 36 micro-sharpened, high aspect-ratio columns with lateral striations on top of a perforated plate and close-up of the side view of a tip.



▲ Figure 2: A monolithic array of 36 3D-printed, micro-sharpened, high aspect-ratio columns with lateral striations on top of a perforated plate with close-up of the side view of a tip and top view of one of the columns. The structure could be used as a multiplexed externally fed electro spray source.

## FURTHER READING

- L. F. Velásquez-García, "SLA 3D-Printed Arrays of Miniaturized, Internally-Fed, Polymer Electro spray Emitters," submitted.
- L. F. Velásquez-García, "Additive manufacturing of electro spray emitter arrays and other microfluidic systems," submitted to USPTO.

# Piezoelectric Nonlinearity in GaN Lamb Mode Resonators

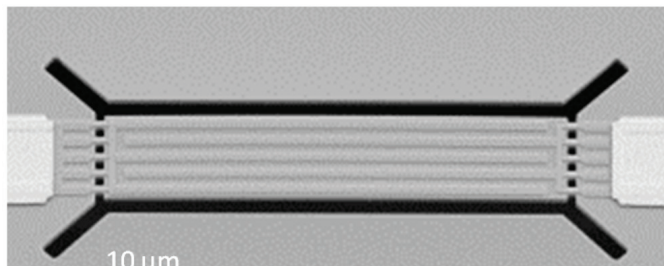
S. Wang, L. Popa, D. Weinstein  
Sponsorship: National Science Foundation, DARPA DAHI

This paper reports on the measurement of nonlinearity in GaN Lamb mode resonators subjected to power levels between 10 and +10 dBm. In these devices, nonlinearity manifests itself as both frequency shift ( $\Delta f/f$  of 60-128 ppm) and change in motional impedance ( $\Delta Rm/Rm$  of 13-33%). In this work, we decouple the contributions from self-heating and strain-induced piezoelectric nonlinearity to  $\Delta R/R$ , and conclude that strain-induced change in piezoelectric coefficients  $\Delta e_{31}$  and  $\Delta e_{33}$  is the dominant cause of  $\Delta R/R$ , accounting for 31% of the total 33% observed shift. The result is consistent with 2nd order nonlinear coefficients previously derived analytically.

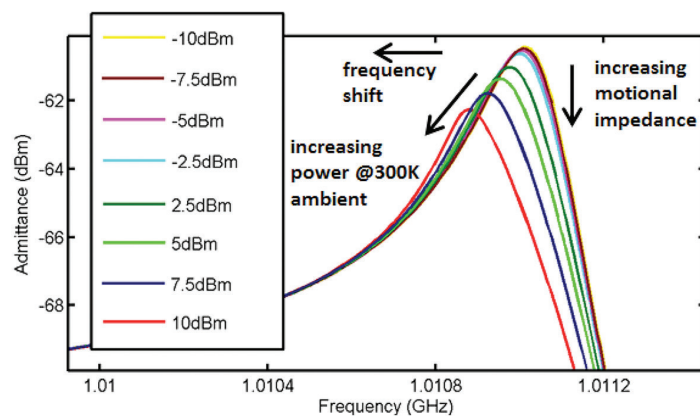
Whether for use in radio filters or in frequency references, the MEMS resonator's capability to handle large RF power is crucial for system performance. It is therefore important to understand any nonlinearity in

piezoelectric MEMS resonators. Studies have shown that self-heating is a primary contributor to frequency shift in AlN Lamb mode resonators. In this paper, we show that GaN Lamb mode resonators (Figure 1) are subject not only to frequency shift ( $\Delta f$ ) from self-heating, but also to an increase in motional impedance ( $\Delta Rm$ ) with increasing power levels due to a significant nonlinearity in piezoelectric coefficients (Figure 2). After ruling out these two factors, we conclude that the amplitude-induced  $\Delta e_{31}$  and  $\Delta e_{33}$  are the dominant contribution to  $\Delta Rm$ , consisting about 31% of the total 33% change.

The paper also concludes that self-heating is the main cause of frequency shift and nonlinearity in piezoelectric coefficient will dominate IIP3 (the input power at the third-order intercept point), an importance specification for weakly nonlinear devices in RF communication



◀ Figure 1: SEM of GaN Lamb mode resonator under study. This corresponds to Device 2 in Figure 3.



◀ Figure 2: 1-port frequency response of GaN Lamb mode resonator, showing frequency drop and motional impedance increase with increasing power levels.

## FURTHER READING

- P.-Y. Prodhomme, A. Beya-Wakata, G. Bester, "Nonlinear piezoelectricity in Wurtzite semiconductors," *Physical Review B* 88(12), 121304 (2013)
- S. Wang, L.C. Popa, D. Weinstein, "GaN MEMS resonator using a folded phononic crystal structure," *IEEE MEMS'15*, pp. 1028-31 (2015).
- A. Tazzoli, M. Rinaldi, G. Piazza, "Experimental investigation of thermally induced nonlinearities in Aluminum Nitride contour-mode MEMS resonators," *IEEE Electron Device Letters* 33(5), 724-726 (2012).

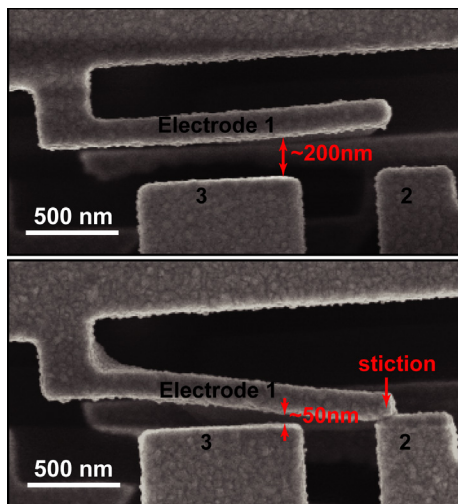
# Controlled Fabrication of Nanoscale Gaps using Stiction

F. Niroui, E. M. Sletten, P. B. Deotare, A. I. Wang, T. M. Swager, J. H. Lang, V. Bulović  
Sponsorship: National Science Foundation Center for Energy Efficient Electronics Science

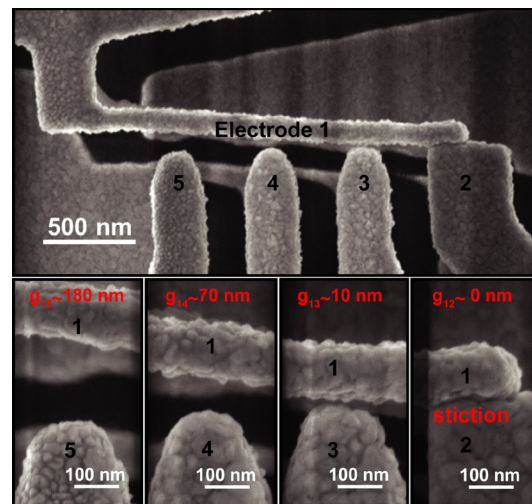
As dimensions are continuously scaled down to achieve devices with higher performance and novel principles, developing methods for the controlled fabrication of nanogaps is important for enabling functional devices. Nanogaps are particularly critical for advancements in nanoelectromechanical systems (NEMS) and molecular electronics. Various methods of fabricating such gaps have been reported in the literature. However, these approaches are developed mainly for two-terminal devices, involve multiple processing steps, and commonly lack robustness, thus limiting their applications.

In this work we present an approach to controlled fabrication of nanoscale gaps through use of stiction, i.e., permanent adhesion between device components, an otherwise common mode of failure in electromechanical systems. In this scheme, laterally actuated cantilevers are patterned through electron beam lithography in polymethyl-methacrylate (PMMA). During the wet-developing process, the cantilever (labeled Electrode 1 in Figure 1) undergoes deflection due to the capillary

forces, permanently adhering (stiction) to the opposing structure (Electrode 2). The deflection and stiction promote formation of nanogaps, smaller than originally patterned, between the cantilever and opposing electrode. Lastly, gold (Au) is evaporated onto the substrate defining the metallic electrodes onto the PMMA structures. The Au evaporation further reduces the gap size depending on the thickness of the film. The extent of deflection and its profile can be controlled through balancing the surface adhesive forces by altering the device geometry such that desired widths are achieved. The tunability of the gap size through device design is shown in Figure 2, where relative placement of the electrode with respect to the point of stiction defines the widths of the gap achieved. Furthermore, through modifications of device design, the nanogaps can be optimized to be electromechanically tunable or filled with molecular layers making them suitable for applications in tunneling electromechanical switches, nanoelectromechanical systems, and molecular electronics.



▲ Figure 1: Stiction induced through capillary forces during the fabrication process promotes formation of nanogaps smaller than patterned through the lithography process.



▲ Figure 2: Optimizing device architecture and electrode placement relative to the point of stiction allows achievement of nanogaps with controlled width.

## FURTHER READING

- F. Niroui, E. M. Sletten, P. B. Deotare, A. I. Wang, T. M. Swager, J. H. Lang, and V. Bulović, "Controlled fabrication of nanoscale gaps using stiction," in *Proc. 28th IEEE International Conference on Micro Electro Mechanical Systems (MEMS)*, 2015, pp. 85-88.
- F. Niroui, P. B. Deotare, E. M. Sletten, A. I. Wang, E. Yablonovitch, T. M. Swager, J. H. Lang, and V. Bulović, "Nanoelectromechanical tunneling switches based on self-assembled molecular layers," in *Proc. 27th IEEE International Conference on Micro Electro Mechanical Systems (MEMS)*, 2014, pp. 1103-1106.

# Printed MEMS Membrane Electrostatic Microspeakers

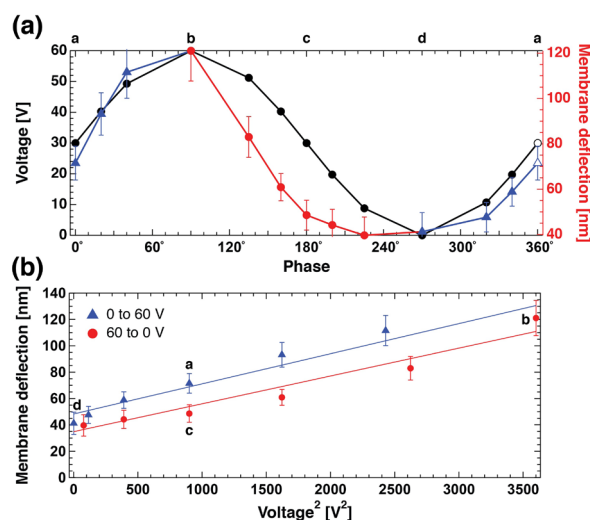
A. Murarka, J. Jean, J. Lang, V. Bulović

Sponsorship: National Science Foundation Center for Energy Efficient Electronics Science

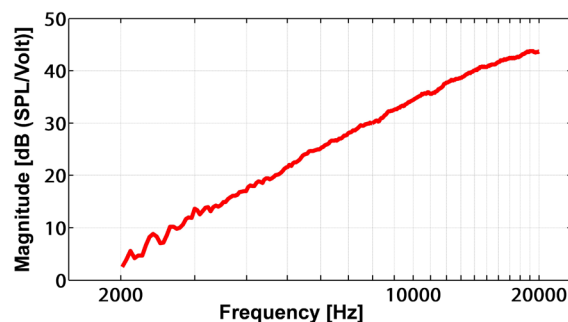
This work reports the fabrication and operation of electrostatic microspeakers formed by contact-transfer of 125-nm-thick gold membranes over cavities patterned in a micron-thick silicon dioxide ( $\text{SiO}_2$ ) layer on a conducting substrate. Upon electrostatic actuation, the membranes deflect and produce sound. Additionally, membrane deflection upon pneumatic actuation can be used to monitor pressure. The microspeaker fabrication process reported enables fabrication of MEMS diaphragms without wet or deep reactive-ion etching, thus obviating the need for etch-stops and wafer-bonding. This process enables monolithic fabrication of multiple completely enclosed drum-like structures with non-perforated membranes to displace air, in both individual-transducer and phased-array geometries.

We characterized the mechanical deflection of the gold membranes using optical interferometry. The membranes show a repeatable peak center deflection of

$121 \pm 13$  nm across gaps of  $\sim 25$  microns at 1 kHz sinusoidal actuation with 60 V peak-to-peak amplitude and a 30 V DC bias (Figure 1). The acoustic performance of the microspeakers is characterized in the free field. Sound pressure level of the microspeaker increases with frequency at 40 dB/decade (Figure 2), indicating that its sound pressure output is proportional to the acceleration of its diaphragm, as expected in the spring-controlled regime for free field radiation. The microspeaker consumes 262  $\mu\text{W}$  of real electric power under broadband actuation in the free field and outputs 34 dB(SPL/Volt) of acoustic pressure at 10 kHz drive. The silicon wafer substrate ( $\sim 500$   $\mu\text{m}$  thick) dominates the total thickness of the microspeakers; the active device thickness is less than 2  $\mu\text{m}$ . These thin microspeakers have potential applications in hearing aids, headphones, and large-area phased arrays for directional sound sources.



▲ Figure 1: Deflection profiles of gold membrane suspended over cavities, obtained via optical interferometry during 1 kHz AC actuation. Center deflections of this membrane over 83 cavities as functions of time were extracted from the profiles and averaged to yield a single deflection time function. That time function and corresponding applied voltage are plotted. (a) Applied voltage (black) and averaged peak membrane deflection (red and blue) are shown as functions of time. (b) Membrane deflections are plotted against square of applied voltage with time as a parameter. Points labeled a-b-c-d-a in (b) indicate position of corresponding points on the periodic deflection and voltage waveforms in (a).



▲ Figure 2: Acoustic frequency response, from 2 kHz to 20 kHz, of a gold membrane microspeaker, 12.5 mm<sup>2</sup> in area. Magnitude of transfer function,  $|T_{pv}|$ , from driving voltage amplitude to sound output measured by the microphone is converted to decibels using 20  $\mu\text{Pa}$  as reference pressure, i.e., magnitude plotted is  $20 \log_{10}(|T_{pv}|/20 \mu\text{Pa})$ .

## FURTHER READING

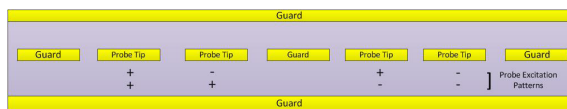
- A. Murarka, A. Wang, J. Jean, J. H. Lang, and V. Bulović, "Printed MEMS membrane electrostatic microspeakers," in *Solid-State Sensors, Actuators and Microsystems Workshop, Hilton Head Island, South Carolina*, 2014, pp. 311-314.
- A. Murarka, S. Paydavosi, T. L. Andrew, A. I. Wang, J. H. Lang, and V. Bulović, "Printed MEMS membranes on silicon," in *IEEE 25th International Conference on Micro Electro Mechanical Systems (MEMS)*, 2012, pp. 309-312.
- A. Murarka, C. Packard, F. Yaul, J. Lang, and V. Bulović, "Micro-contact printed MEMS," in *IEEE 24th International Conference on Micro Electro Mechanical Systems (MEMS)*, 2011, pp. 292-295.

# Electromagnetic Imaging of Nanostructures

R. Kumar, T. Hamer, D. L. Trumper, J. H. Lang  
Sponsorship: Lincoln Laboratory

This objective of this project is to develop a system to perform high bandwidth, subsurface, electromagnetic imaging of microfabricated devices. The intent is to simultaneously detect surface topologies, buried conductors/insulators, and doped regions. The proposed system promises to offer very high measurement bandwidth, enabling rapid measurement of large areas with high resolution which is critical to the time-efficient scanning of complex semiconductor wafers.

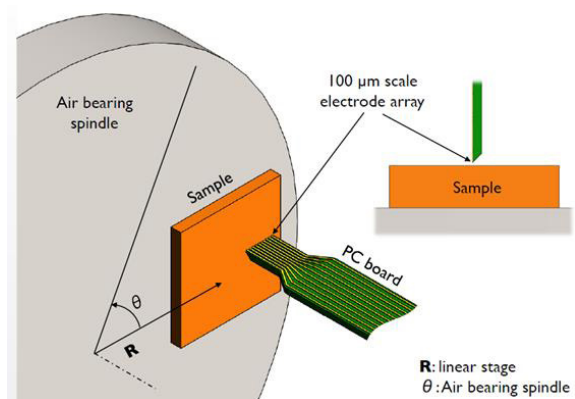
Our imaging approach is based on high-frequency impedance measurements through an array of electrodes capacitively coupled to a microfabricated device. As the electrode array is scanned over the device surface, the resulting impedance variations will be measured and transformed into a 3D tomographic map of the near-surface spatial distributions of the sample permittivity and conductivity. Also, nonlinearities in the current/voltage relationship of P-N junctions allow detection of the dopant boundaries by measuring the harmonic distortion. We plan to drive the electrodes with GHz excitation frequencies, and maintain the electrode array at a submicron flying height above the semiconductor surface. High excitation frequencies are necessary for the electric field generated from the sensor array to penetrate the silicon substrate in sufficient depth, thereby being coupled to the sub-surface features.



▲ Figure 1: Cut away, side view of MEMS probe head. Details the different excitation patterns applied to each probe tip and the placement of the guards to avoid interference of fringing fields.

The imaging system will consist of a MEMS probe head, precision mechatronics, and RF electronics. The probe head will be fabricated from an array of gold electrodes that will be sandwiched between guard electrodes to prevent stray fields from interfering with the capacitance measurement; see Figure 1 for details. These probes will then fan out back to a vector network analyzer (VNA) which measures the impedance of each probe tip at high frequencies (0.5 GHz – 6 GHz). Different excitation patterns may be applied from the VNA to the gold probes to control the depth of penetration of the electric fields into the nanostructure to be imaged. RF electronics will be used to mitigate losses at high frequencies while guarding against unwanted stray electric fields. Finally, an inverting imaging algorithm will be developed to compute a final image from the measured impedance data.

For the experimental setup, the test sample is mounted onto an air bearing spindle and the probe will be placed perpendicularly to the sample, as in Figure 2. Next, the spindle is rotated at a predefined angular velocity and the change in impedance, as the probe tip passes over the test sample, is measured by the RF equipment. After the data is collected, it is processed using the inverse imaging algorithm to output a map of the material composition of the test structure.



▲ Figure 2: Diagram of the experimental setup detailing the placement of the probe head in relation to the sample.

## FURTHER READING

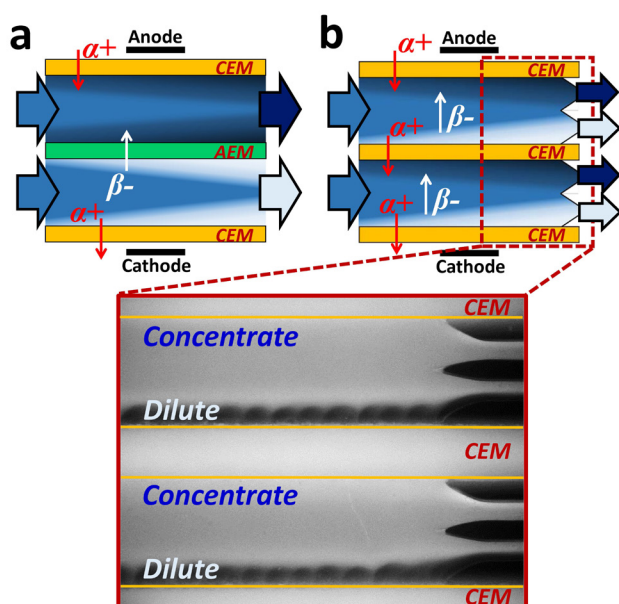
- B. L. Cannon, "Electroquasistatic Sensors for Surface and Subsurface Nano-Imaging of Integrated Circuit Features," Master's Thesis, Massachusetts Institute of Technology, Cambridge, 2010.
- Agilent Technologies, Appl. Note 5989-8818 Rev A.

# Purification of High Salinity Brine by Multi-Stage Desalination via Ion Concentration Polarization (ICP)

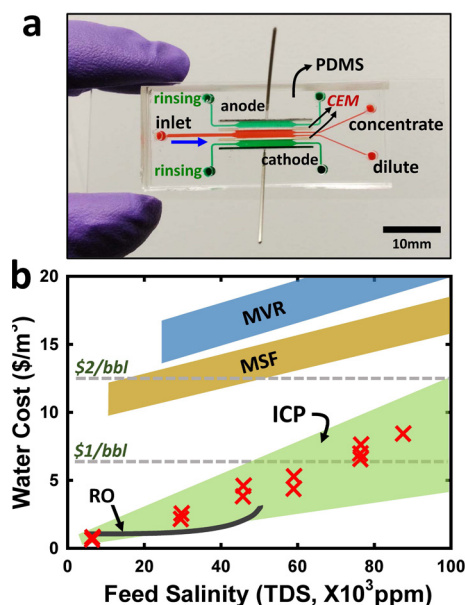
B. Kim, V. S. Pham, J. Han  
Sponsorship: ARPA-E

There is an increased need for the desalination of high concentration brine (> TDS 35,000ppm) efficiently and economically, either for the treatment of produced water from shale gas/oil development, or minimizing the environmental impact of brine from existing desalination plants. Although electro-membrane desalination (e.g., electrodialysis) has been underestimated and considered as a limited technology for brackish water treatment, we have found its multiple advantages for brine treatment. Based on our earlier works (Figure 1) showing better salt removal and energy efficiency than conventional electrodialysis (ED), we demonstrate technical and economic viability of ion concentration

polarization (ICP) electrical desalination for the high saline water treatment by adopting a novel multi-stage operation. According to our analysis with a miniaturized microfluidic platform (Figure 2a), one can achieve competitive water cost (~\$1/bbl) of highly concentrated brine desalination by optimizing the energy use by adopting the strategy of incremental, multi-stage salt removal in electrical desalination (Figure 2b). We also demonstrate that ICP desalination has the advantage of removing both salts and diverse suspended solids simultaneously, and of less susceptibility to membrane fouling/scaling, which is a significant challenge in any membrane processes.



▲ Figure 1: Schematic view of electrical membrane desalination. (a) (ED) and (b) (ICP) desalination with fluorescent image. Red and white arrows indicate the movement of cation  $\alpha+$  and anion  $\beta-$  by electric field, respectively. Bright and dark regions in schematic figures represent ion-depleted and ion-enriched region, respectively; the fluorescent image shows an opposite contrast.



▲ Figure 2: (a) Photo of PDMS-based microfluidic ICP desalination device and (b) Cost analysis of ICP desalination. 12 red X denote results of ICP desalination based on the experiments with fixed recovery of 0.5 and 70-75% salt removal ratio from various feed salinity (5,800-87,700 mg/L of TDS, equivalent to 0.1-1.5M NaCl solution), where most flowback and some produced water range.

## FURTHER READING

- K. B. Gregory, R. D. Vidic, and D. A. Dzombak, "Water Management Challenges Associated with the Production of Shale Gas by Hydraulic Fracturing", *Elements*, vol. 7, pp. 181-186, June 2011.
- R. Kwak, V. S. Pham, B. Kim, L. Chen, and J. Han, "High-Throughput Salt/Bio-Agent Removal by Ion Concentration Polarization for Water Desalination," in *Proc. International Conference on Miniaturized Systems for Chemistry and Life Sciences*, 2013, pp. 660-662.
- B. Kim, R. Kwak, H. J. Kwon, V. S. Pham, S. E. Kooi, G. Lim, and J. Han, "Purification of Ultra-High Salinity Produced Water by Multi-Stage Ion Concentration Polarization," in *Proc. International Conference on Miniaturized Systems for Chemistry and Life Sciences*, 2014, pp. 160-162.

# Enhanced Flow Boiling in Microchannels via Incorporated Surface Structures

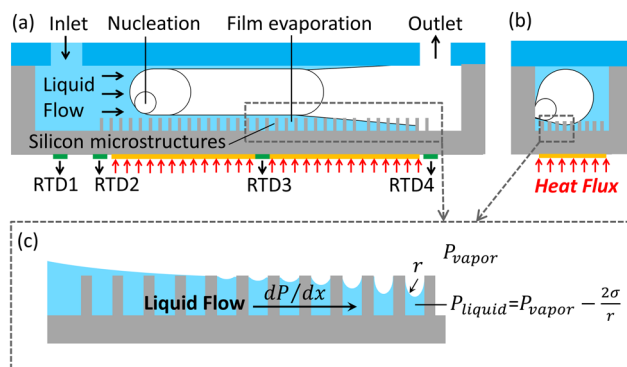
Y. Y. Zhu, D. S. Antao, D. W. Bian, E. N. Wang

Sponsorship: Masdar Institute of Science and Technology, Battelle Memorial Institute, Air Force Office of Scientific Research

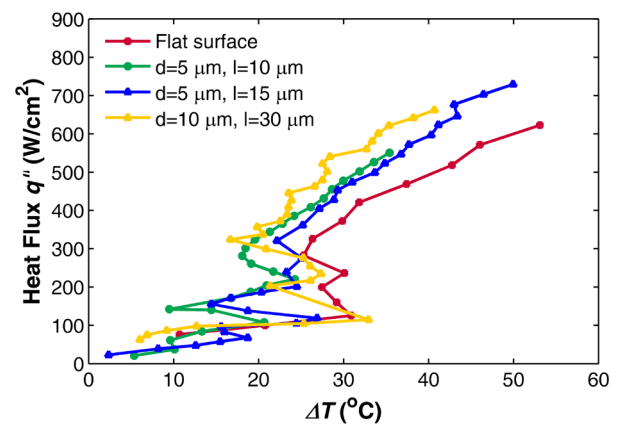
The increasing power densities in various electronic devices including concentrated photovoltaics, power electronics, and laser diodes pose significant thermal management challenges for the electronics industry. The use of two-phase microchannel heat sinks to cool high-performance electronic devices is attractive because they harness the latent heat of vaporization to dissipate high heat fluxes in a compact form factor. However, the challenges with such a scheme are associated with flow instability and the need to increase the critical heat flux (CHF), which is the highest heat flux the device is capable of dissipating before heat transfer failure.

Recently, incorporating micro/nanostructures onto the surfaces of the microchannels has opened up new opportunities for performance enhancement. Here we investigate the role of surface microstructures on flow boiling heat transfer in microchannels. We designed and fabricated microchannels with well-defined silicon micropillar arrays (heights of  $\sim 25 \mu\text{m}$ , diameters of  $5\text{-}10 \mu\text{m}$  and pitches of  $10\text{-}30 \mu\text{m}$ ) on the bottom heated

channel wall. The design decouples thin film evaporation and nucleation by promoting capillary flow on the bottom heated surface while facilitating nucleation from the sidewalls. The structured surface microchannels showed significantly reduced temperature and pressure drop fluctuation. Visualization of the flow indicates that the micropillar surface can promote capillary flow and enhance flow stability and heat transfer by maintaining a stable annular flow, which resulted in high-performance thin film evaporation and an enhanced critical heat flux. The fabricated devices achieved significantly enhanced heat transfer coefficient (40%) compared to that without micropillars, and a maximum CHF value of  $720 \text{ W/cm}^2$  was achieved on a structured surface microchannel (diameters of  $5 \mu\text{m}$  and pitches of  $15 \mu\text{m}$ ). The experimental results suggest that capillary flow can be maximized without introducing large viscous resistance when the microstructure geometry is optimized. This work is a first step towards guiding the design of stable, high-performance two-phase microchannel heat sinks.



▲ Figure 1: Schematic of microchannel heat sink design with micropillars on the heated surface. (a) Side view, (b) cross-section view, and (c) magnified view of the liquid film forming menisci that create capillary pressure gradient to help drive the liquid flow. The equation that describes the liquid pressure under a meniscus is the Young-Laplace equation, where  $\sigma$  is the surface tension of the liquid,  $r$  is the radius of curvature of the local meniscus, and  $P_{liquid}$  and  $P_{vapor}$  are the local pressure of the liquid and vapor, respectively.



▲ Figure 2: Heat transfer performance characteristics of the microchannel. Heat flux  $q''$  vs. microchannel backside surface temperature rise  $\Delta T$ . The maximum point on each curve indicates the critical heat flux, which is the highest heat flux the device is capable of dissipating before heat transfer failure. Error bars for  $q''$  were approximately  $\pm 1\%$ . Error bars for  $\Delta T$  were approximately  $\pm 3.5 \text{ }^\circ\text{C}$  for the structured devices and grew with the heat flux due to the increasing temperature oscillations ( $\pm 3.5 \text{ }^\circ\text{C}$  to  $\pm 11 \text{ }^\circ\text{C}$ ) for the smooth surface microchannel.

## FURTHER READING

- Y. Y. Zhu, D. S. Antao, K.-H. Chu, T. J. Hendricks, and E. N. Wang, "Enhanced Flow Boiling Heat Transfer in Microchannels with Structured Surfaces," presented at International Heat Transfer Conference, Kyoto, Japan, 2014. Doi: 10.1615/IHTC15.nms.009508

# Experimental Characterization of Thin-Film Evaporation from Silicon Micropillar Wicks

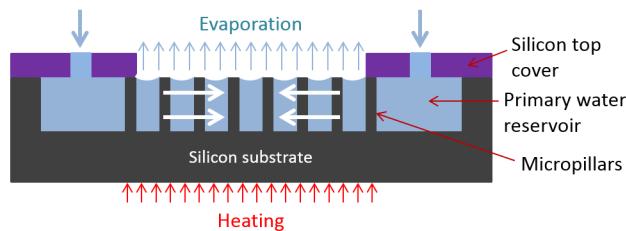
S. Adera, D. S. Antao, R. Raj, E. N. Wang

Sponsorship: Office of Naval Research with Mark Spector as program manager, National Science Foundation Graduate Research Fellowship Program

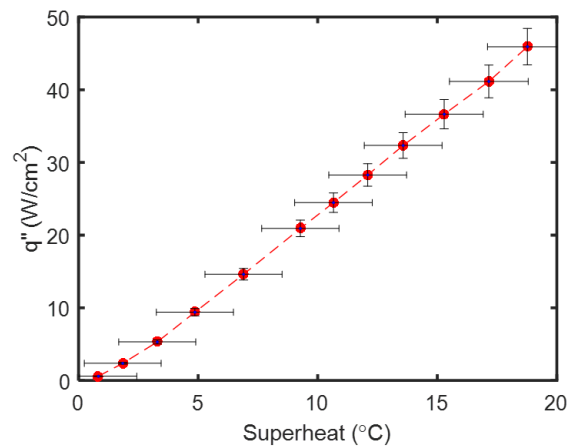
To the credit of Moore's Law, the exponential rise in the number of transistors in a single chip, the increase in clock speed and functionality, and the continual overall size reduction in device architecture of electronic devices have generated concentrated heat loads in excess of  $100 \text{ W/cm}^2$ . Furthermore, this heat flux is projected to exceed  $300 \text{ W/cm}^2$  in a few years [1] creating a thermal management challenge. While enhanced air convection cooling strategies have done the job in the past, direct extension of the state-of-the-art air cooling technology is inadequate to remove heat loads in excess of  $100 \text{ W/cm}^2$ . As a result, novel thermal management solutions such as thin-film evaporation [2] that utilize the latent heat of vaporization as the working fluid changes phase from liquid to vapor are required to mitigate this thermal management challenge.

In this work, we have experimentally characterized thin-film evaporation from silicon micropillar wicks. The micropillars were created using contact photolithography and deep-reactive ion etching. For integrated testing and measurement, a thin-film heater and microsensors were incorporated using e-beam evaporation and acetone lift-off. The microsensors measure local temperature while the heater emulates

the heat generated in electronic devices. The experiment was conducted in a vacuum chamber and de-ionized water was passively transported to the evaporator surface via capillary-wicking (Figure 1). The water was syphoned into the microstructured surface from the surrounding reservoir in response to the input heat flux. Steady state thin-film evaporation in the absence of nucleate boiling was demonstrated. The liquid meniscus recedes and the microstructured surface dries out when the capillary wicking mechanism cannot deliver sufficient liquid to sustain the evaporation by overcoming viscous losses. Dryout heat fluxes of  $\approx 46 \text{ W/cm}^2$  were dissipated at  $19^\circ\text{C}$  superheat (Figure 2) over a  $1\text{cm} \times 1\text{cm}$  microstructured area and the effects of micropillar wick geometry were captured through systematic study. Experimental results show that the dryout heat flux scales with micropillar wick thickness. Furthermore, for a given micropillar wick thickness, an optimum pillar diameter and spacing is identified which maximizes the capillary-limited evaporation dryout heat flux. Our study provides mechanistic understanding of the liquid transport and heat transfer processes of thin-film evaporation from well-defined micropillar wicks.



▲ Figure 1: Schematic of device concept. Variation in the liquid meniscus shape from edge of microstructured area to the center creates a pressure gradient that can be used for transporting liquid passively via capillary-wicking. Liquid is delivered to the microstructured area by overcoming the viscous loss. When the viscous loss exceeds the capillary pressure, a dry island is created at the center of the microstructured area which grows radially outwards. Liquid lost through evaporation from top liquid-vapor interface is replenished at the base of the micropillar wick.



▲ Figure 2: Heat flux as a function of superheat. Last data point is the dryout heat flux beyond which the rate of evaporation exceeds the amount of water delivered via capillary-wicking.

## FURTHER READING

- J. R. Thome, "The new frontier in heat transfer: microscale and nanoscale technologies," *Heat Transf Eng*, vol. 27, no. 9, pp. 1-3 (2006).
- M. Potash Jr and P. Wayner Jr, "Evaporation from a two-dimensional extended meniscus," *Int J Heat Mass Transf*, vol. 15, no. 10, pp. 1851-1863 (1972).

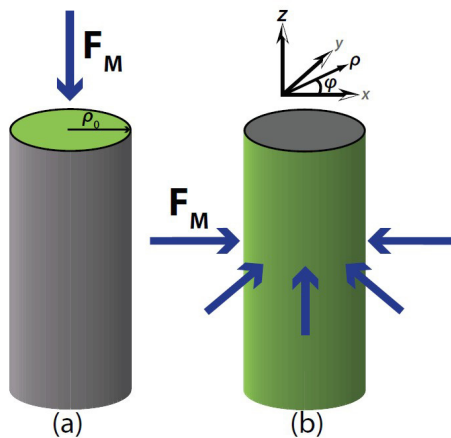
# Elementary Framework for Cold Field Emission: Emission from Quantum-Confined Emitters

A. A. Patterson, A. I. Akinwande  
Sponsorship: DARPA, National Science Foundation GRFP

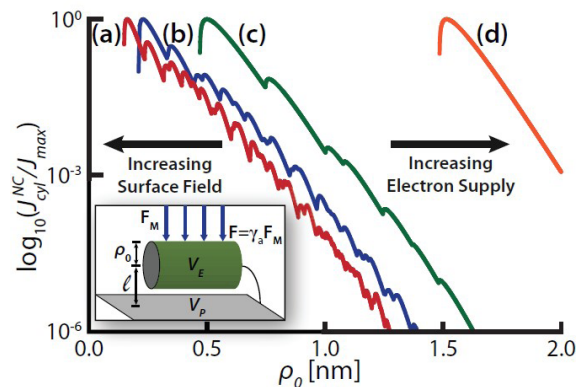
Cold field emission is the emission of electrons from a metal at  $T=0\text{K}$ , induced by an electrostatic field. Field emitted current density (ECD) is traditionally predicted with the Fowler-Nordheim (FN) equation, which assumes a bulk, planar, metal emitter. Due to the enhancement of a static electric field at highly curved surfaces (lightning rod effect), the conventional strategy for increasing the ECD is to fabricate ever smaller and more highly-curved emitter tips. However, for suitably small field emitters, the effects of quantum confinement (QC) at the emitter tip may play a significant role in determining the total ECD since the specific shape of a quantum system determines its electronic wave functions and distribution of energy levels. In order to study the competing effects of a reduced electron supply due to QC and increased electron transmission probability from local field enhancement, our previously developed elementary framework for cold field emission has been reformulated to treat emission from non-planar surfaces of QC metal emitters.

The framework was employed to derive ECD equations for emission from the planar surface of a

normally unconfined (NU) 1D cylindrical nanowire (CNW) and the curved side of a normally confined (NC) 1D CNW, which are illustrated in Figure 1. The energy level spacing, energy level degeneracy, and transverse zero-point energy unique to each emitter geometry led to certain geometries producing larger ECDs than others under equivalent conditions. The close energy level spacing and lack of a transverse zero-point energy in the NC CNW geometry led to exceptionally large ECD peaks, an average ECD that exceeded the FN limit at typical values of  $E_F$ , and an increasing trend in the ECD with decreasing emitter dimensions in the presence of field enhancement, which is shown in Figure 2. These results suggest that highly curved emitter geometries may be ideal for emission from the standpoint of not only tip electrostatics, but also the electron supply. Current work includes the application of the framework to more realistic emitter tip geometries, such as paraboloids, and the development of an analogous framework for emission from non-planar, quantum-confined semiconductor emitters.



▲ Figure 1: Emission from a (a) normally unconfined 1D cylindrical nanowire emitter and a (b) normally confined 1D cylindrical nanowire emitter.  $\rho_0$  is the emitter radius,  $F_M$  is the applied electric field, and  $e^-$  are the emitted electrons.



▲ Figure 2: In the presence of local field enhancement, the normalized ECD from the NC CNW emitter  $J_{cyl}^{NC}/J_{max}$  increases as a function of decreasing emitter radius  $\rho_0$ , for Fermi energy values of (a) 10 eV, (b) 5 eV, (c) 1 eV, and (d) 0.1 eV. The increasing electric field at the emitter surface increases electron transmission probability more rapidly than QC reduces the spatial density of electrons available to tunnel as  $\rho_0$  decreases.

## FURTHER READING

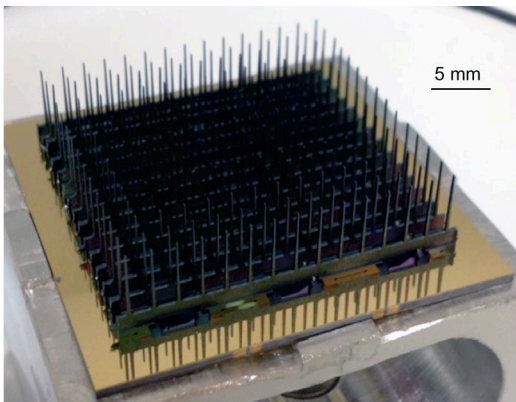
- R. H. Fowler and L. Nordheim, "Electron Emission in Intense Electric Fields," in *Proc. Royal Soc. of London. Series A, Containing Papers of a Math. and Phys. Character*, vol. 119, no. 781, pp. 173-181, Mar. 1928.
- A. A. Patterson and A. I. Akinwande, "Elementary Framework for Cold Field Emission: Incorporation of Quantum-Confinement Effects," *Journal of Applied Physics*, vol. 114, no. 23, p. 234303, Dec. 2013.

# High-Throughput Manufacturing of Nanofibers using Planar Arrays of Microfabricated Externally Fed Emitters

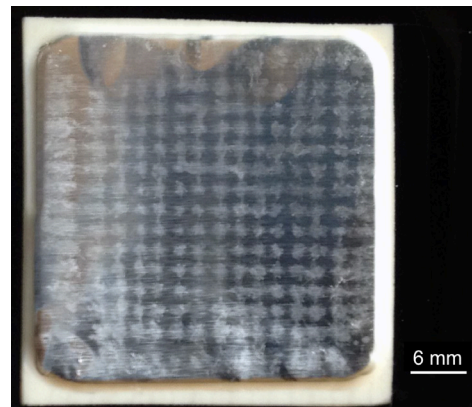
P. J. Ponce de Leon, F. A. Hill, L. F. Velásquez-García  
Sponsorship: DARPA

Electrohydrodynamic jetting occurs when a strong electric field is applied to the free surface of a conductive liquid; the process can uniformly produce ion plumes, fine aerosol droplets, or continuous fibers with sub-micron diameters, i.e., nanofibers, depending on the properties of the liquid used and the ionization conditions. Nanofabrication via electrohydrodynamic jetting has received attention as a promising candidate for production of nanostructures because of its ability to create nano-thick films of high quality at lower temperature than standard solid-state processing. A key advantage of electrospinning, i.e., electrohydrodynamic jetting of nanofibers, over other fiber generation methods is its versatility in producing fibers of arbitrary length from a range of materials including polymers, metals, ceramics, and semiconductors. The applications of electrospun nanofibers include dye-sensitized solar cells, scaffolds for tissue engineering, electrodes for ultracapacitors, and separation membranes.

We created a technology for high-throughput generation of polymer nanofibers using planar arrays of microfabricated externally fed electrospinning emitters. Devices with emitter density as high as 25 emitters/cm<sup>2</sup> (Figure 1) deposit uniform imprints comprising fibers with diameters on the order of a few hundred nanometers using solutions of dissolved polyethylene oxide in water and ethanol as working fluid (Figure 2). We measured mass flux rates as high as 417 g/hr/m<sup>2</sup>, i.e., 4x the reported production rate of leading commercial free-surface electrospinning sources. Throughput increases with increasing array size at constant emitter density, showing that the design can be scaled up with no loss of productivity. The largest measured mass flux resulted from arrays with larger emitter separation operating at larger bias voltages, indicating the strong influence of electrical field enhancement on the performance of the devices. Inclusion of a ground electrode surrounding the array tips helps control the spread of the imprints over large distances.



▲ Figure 1: An array of 15×15 externally fed electrospinning emitters (25 emitters/cm<sup>2</sup>). From P. Ponce de Leon et al., *Nanotechnology*, vol. 26, no. 22, 225301 (10 pp.), June 2015.



▲ Figure 2: Collector imprints from an array of 225 emitters (25 emitters/cm<sup>2</sup>). From P. Ponce de Leon et al., *Nanotechnology*, vol. 26, no. 22, 225301 (10 pp.), June 2015.

## FURTHER READING

- P. Ponce de Leon, F. A. Hill, and L. F. Velásquez-García, "Batch-Microfabricated Arrays of Electrospinning Emitters for High Throughput Generation of Nanofibers," *Technical Digest 12th International Workshop on Micro and Nanotechnology for Power Generation and Energy Conversion Applications (PowerMEMS 2012)*, Dec., 2012, pp. 227 – 230.
- Ponce de Leon, F. A. Hill, E. V. Heubel, and L. F. Velásquez-García, "High-Throughput Manufacturing of Polymer Nanofibers via Electrohydrodynamic Jetting from Planar Arrays of Microfabricated Externally-Fed Emitters," presented at the *18th International Conference on Solid-State Sensors, Actuators, and Microsystems (Transducers 2015)*, Anchorage AK, June 2015.
- P. Ponce de Leon, F. A. Hill, E. V. Heubel, and L. F. Velásquez-García, "Parallel Nanomanufacturing via Electrohydrodynamic Jetting from Microfabricated Externally-Fed Emitter Arrays," *Nanotechnology*, vol. 26, no. 22, 225301 (10 pp.), June 2015.

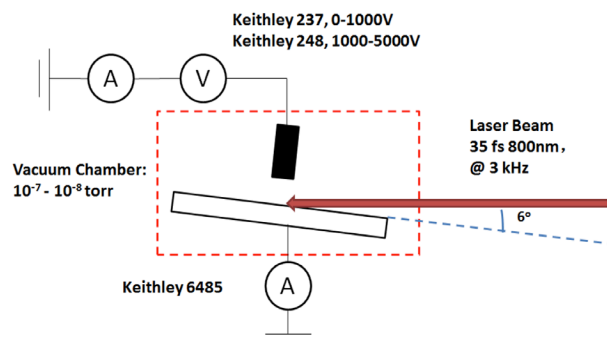
# Optimization of the Morphology of Arrays of Nano-Sharp, Photon-Triggered Silicon Field Emitters to Maximize their Total Current Emission

C. D. Dong, M. E. Swanwick, P. D. Keathley, F. X. Kärtner, L. F. Velásquez-García  
Sponsorship: DARPA

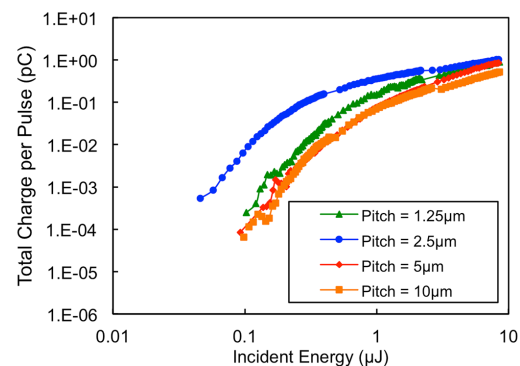
Femtosecond ultrabright cathodes with spatially structured emission are a critical technology for applications such as free-electron lasers, tabletop coherent x-ray sources, and ultrafast imaging. State-of-the-art UV photocathodes have several disadvantages: (i) they need to be fabricated, stored, and operated in ultra-high vacuum and (ii) producing high current pulses reduces their lifetime due to the rapid degradation of the low workfunction material. Cathodes based on photon-triggered field emission, i.e., tunneling of electrons due to the interaction of high-intensity optical pulses with field enhancing structures, are a promising technology to bypass these shortcomings. We recently reported batch-fabricated photon-triggered field emission cathodes composed of massively multiplexed arrays of nano-sharp high-aspect-ratio silicon pillars; the devices are made using standard complementary metal-oxide semiconductor batch fabrication processes, are stored at atmospheric conditions, and can be operated at lower vacuum levels than standard photocathodes with no degradation. The devices are capable of pC-level emission with multi-kHz repetition, greatly increasing the total emitted charge per pulse compared

to single-emitter sources. Through experiment and simulations, this work explores the optimization of the total electron yield of ultrafast photon-triggered field emission cathodes composed of arrays of nanosharp, high-aspect-ratio, single-crystal silicon pillars by varying the emitter pitch and height.

Arrays of 6-nm-tip-radius silicon emitters with emitter densities between 1.2 and 73.9 million tips.cm<sup>-2</sup> and emitter height between 2.0 μm and 8.5 μm were characterized using 35-fs 800-nm laser pulses (Figure 1). Of the devices tested, the arrays with emitter pitch equal to 2.5 μm produced the highest total electron yield; arrays with larger emitter pitch suffer area sub-utilization; and in devices with smaller emitter pitch, the larger emitter density does not compensate for the smaller per-emitter current due to the electric field shadowing that results from the proximity of the adjacent tips (Figure 2). Experimental data and simulations suggest that 2-μm-tall emitters achieve practical optimal performance as shorter emitters have visibly smaller field factors due to the proximity of the emitter tip to the substrate, and taller emitters show marginal improvement in the electron yield at the expense of greater fabrication difficulty.



▲ Figure 1: Schematic of the experimental apparatus used to characterize the photon-triggered silicon field emitter arrays.



▲ Figure 2: Total emitted charge per pulse vs. incident laser pulse energy for devices with emitter pitch equal to 1.25 μm, 2.5 μm, 5 μm, and 10 μm and emitter height equal to 8.5 μm. From C. Dong et al., *Nanotechnology*, vol. 26, no. 26, 265202 (11pp), 2015.

## FURTHER READING

- M. Swanwick, P. D. Keathley, A. Fallahi, P. R. Krogen, G. Laurent, F. X. Kärtner, and L. F. Velásquez-García, "Nanostructured Ultrafast Silicon-Tip Optical Field Emitter Arrays," *Nano Letters*, vol. 14, no. 9, pp. 5035-5043, Jul. 2014.
- P. D. Keathley, A. Sell, W. P. Putnam, S. Guerrero, L. F. Velásquez-García, and F. X. Kärtner, "Strong-Field Photo-Emission From Silicon Field Emitter Arrays," *Annalen Der Physik*, vol. 525, nos. 1-2, pp. 144-150, Feb. 2013.
- C. Dong, M. E. Swanwick, D. Keathley, F. X. Kärtner, and L. F. Velásquez-García, "Multiplexing and Scaling-Down of Nanostructured, Photon-Triggered Silicon Field Emitter Arrays for Maximum Total Electron Yield," *Nanotechnology*, vol. 26, no. 26, 265202 (11pp), Jun. 2015.

## Advanced X-Ray Sources for Absorption Imaging of Low-Z Materials

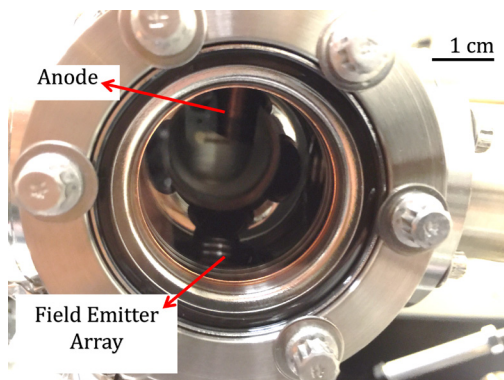
A. Basu, M. E. Swanwick, A. A. Fomani, L. F. Velásquez-García  
Sponsorship: DARPA

X-rays are widely used in applications such as healthcare, airport security, crystallography, spectroscopy, and micro-fabrication. The development of miniaturized X-ray sources could satisfy applications where the target areas are small or where the smaller dimensions and lighter weight of the X-ray source enable desirable capabilities such as portability. For example, compact X-ray sources can revolutionize computerized tomography (CT) by making possible the implementation of a system with multiple X-ray sources that provides a wide range of information without the need to implement a rotating gantry.

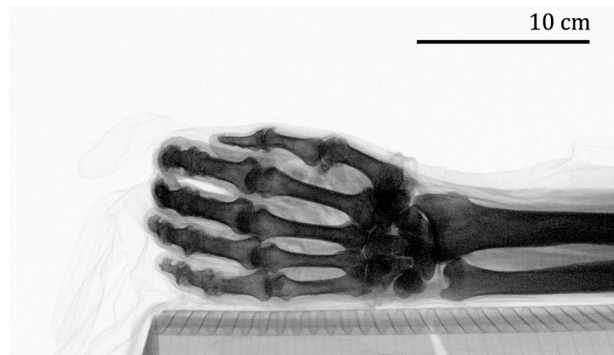
A field emission cathode is an attractive alternative to a conventional thermionic cathode as an electron source in a portable X-ray source because of the lower vacuum it requires to operate, its faster response, and its resilience to traces of reactive gases. Field emission cathodes use high-surface electric fields on the emitter tip surface to narrow the potential barrier that traps electrons in the material, allowing electrons to quantum tunnel into vacuum. Miniaturization and multiplexing of field emitters result in nanostructured field-emitter arrays capable of high-current emission at a low ( $< 150$  V) voltage. The field emitters used in our X-ray source are capable of generating mA-level dc currents even when operated continuously for many hours. High-current cathodes make it possible to capture images in a short time, which helps to reduce any blurriness of the image due to movement of the sample. X-rays generated from a target anode can be categorized

as either bremsstrahlung or fluorescent. On the one hand, bremsstrahlung X-rays span the entire energy range of the bombarding electrons with the maximum energy being determined by the voltage applied to the anode. On the other hand, fluorescent X-rays are characteristic of the target material and appear as specific sharp peaks in the X-ray spectrum. While bremsstrahlung X-rays give rise to low-contrast polychromatic images, fluorescent X-rays could be used to produce quasi-monochromatic, high-contrast images.

For over four years our group has developed advanced field-emission-enabled, near-monochromatic X-ray sources capable of imaging soft tissue structures. Our latest development is a portable X-ray source (200 cm<sup>3</sup> chamber size) with a reflection anode composed of a copper rod coated with a molybdenum thin film and a field emission cathode (Figure 1). A 25 l/s portable ion pump keeps the chamber base pressure at approximately  $10^{-8}$  Torr. At an anode bias voltage of 35 kV, the X-ray source maximizes the percentage of photons with 17.8 keV, which corresponds to the  $K\alpha$  peak of Mo; these X-rays are energetic enough to go through air without significant attenuation ( $\sim 95\%$  transmission) but are of low-enough energy to generate high-contrast absorption images when interacting with soft tissue. Using the X-ray source, we obtained absorption images of ex-vivo samples captured on a CsI scintillator operated in fluoroscopic mode (Figure 2). Features as low as 160  $\mu\text{m}$  were visible in the images.



▲ Figure 1: The inside of the X-ray chamber as seen through a glass port. The field emitter array is hidden from view



▲ Figure 2: Absorption X-ray image of ex vivo human hand captured with anode bias voltage equal to 35 kV and cathode current of 250  $\mu\text{A}$  for 60 seconds of exposure time.

### FURTHER READING

- S. Cheng, F. A. Hill, E. V. Heubel, and L. F. Velásquez-García, "Low-Bremsstrahlung X-ray Source Using a Low-voltage High-current-density Nanostructured Field Emission Cathode And a Transmission Anode For Markerless Soft Tissue Imaging," *Journal of Microelectromechanical Systems*, vol. 24, pp. 373-383, 2015.
- A. Basu, M. Swanwick, A. Fomani, and L. Velásquez-García, "A Portable X-Ray Source With a Nanostructured Pt-coated Silicon Field Emission Cathode For Absorption Imaging of Low-Z Materials," *Journal of Physics D: Applied Physics*, vol. 48, pp. 225501, 2015.

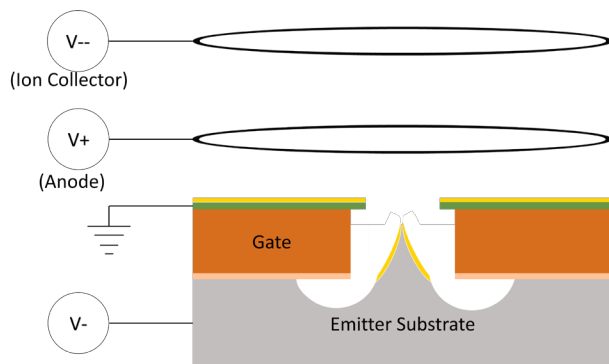
# A Field Emission-Based Ultra-High Vacuum Pump for Cold-Atom Interferometry Systems

A. Basu, M. A. Perez (ColdQuanta, Inc.), L. F. Velásquez-García  
Sponsorship: DARPA

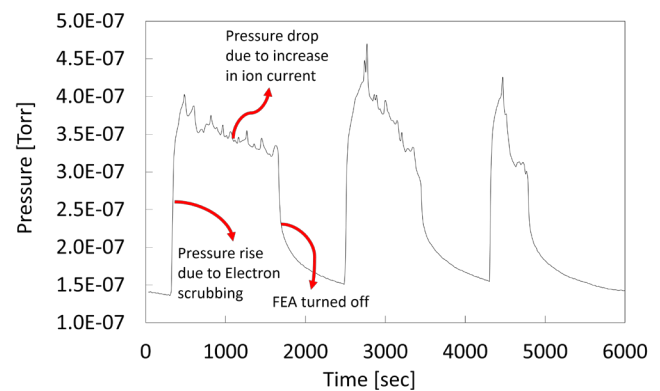
The discovery of magneto-optical trapping of alkali metal vapors in the late 1980s generated a strong interest in developing miniaturized atomic clocks and sensors based on cold alkali atom interferometry. Chip-scale, high-precision atomic sensors can be used in a great variety of exciting applications including fundamental scientific discovery (e.g., general relativity and geophysics), inertial navigation (e.g., gyroscopes and accelerometers), and geological survey (e.g., magnetometers and gravimeters). Cold-atom interferometry needs ultra-high vacuum (UHV, pressure  $< 10^{-9}$  Torr) to operate; therefore, portable cold-atom sensors require miniaturized UHV pump technology compatible with alkali vapor that operates at low power. Standard UHV ion pumps, which use high magnetic fields to increase the ionization probability, are not ideal to maintain vacuum in a chip-scale atomic sensor because the intensity of the magnetic field increases with the reduction in size of the pump and because the magnetic field of the pump can alter the quantum states of the laser-cooled atoms, leading to incorrect measurements. A better alternative is to use an electron source to provide a surplus of electrons to increase the ionization probability, eliminating the need for a magnetic field. A field emission electron source is a good choice for that because, unlike state-of-the-art thermionic cathodes, they do not require high temperature to operate, which makes

them compatible with the reactive alkali environment inside atomic vapor cells.

We preliminarily demonstrated a magnetic-less ion pump design (Figure 1) that uses field electron emission to create a self-sustained plasma within a 200 cm<sup>3</sup> vacuum chamber. A silicon-based, nanostructured, self-aligned, gated field emitter array (FEA) is used as electron source. Two electrodes, both consisting of structural rings wrapped with titanium wire, are placed above the FEA and biased at voltages that enable collection of either electrons or ions. The ion collector is the getter of the pump, capturing the ions both physically (bombardment) and chemically (chemisorption). The apparatus has a rubidium dispenser for releasing the alkali metal vapor inside the chamber, and the chamber is connected to an external pump system capable of maintaining a base pressure of  $\sim 10^{-8}$  Torr within the chamber. The performance of the field emission cathode did not deteriorate due to the presence of Rb at pressures as high as  $7 \times 10^{-6}$  Torr. The pump performance is shown in Figure 2. An initial rise in pressure (due to electron scrubbing) was followed by a 25% drop in pressure (from  $4.0 \times 10^{-7}$  Torr to  $3.0 \times 10^{-7}$  Torr) when the ion current was increased from 0 to 0.5 nA (by increasing the bias on the negatively charged ion collector). Current work focuses on the optimization of the electron impact ionization process to improve pumping performance.



▲ Figure 1: Schematic of the pump architecture. The FEA is represented by a single emitter tip; the anode and ion collectors are ring-shaped structures.



▲ Figure 2: Chamber pressure vs. time. From “Nanostructured Silicon Field Emitter Array-Based High-Vacuum Magnetic-Less Ion Pump for Miniaturized Atomic Spectroscopy Sensors,” *Transducers 2015*, Anchorage AK, June 2015.

## FURTHER READING

- A. Basu, M. A. Perez, and L. F. Velásquez-García, “Nanostructured Silicon Field Emitter Array-Based High-Vacuum Magnetic-Less Ion Pump For Miniaturized Atomic Spectroscopy Sensors,” 18th International Conference on Solid-State Sensors, Actuators and Microsystems (Transducers 2015), Anchorage AK, June 2015.

